Key Engineering Materials
ISSN: 1662-9795, Vol. 926, pp 2004-2011
doi:10.4028/p-67326d

Submitted: 2021-12-08
Revised: 2022-01-26
Accepted: 2022-01-28
Online: 2022-07-22

Periodic Homogenization in Crystal Plasticity: A Comparative Study Between 3D and 2D

Shahrzad Mirhosseini[1,a*], Semih Perdahcıoğlu[1,b], Celal Soyarslan[1,c], and Ton van den Boogaard[1,d]

Chair of Nonlinear Solid Mechanics, Faculty of Engineering Technology, University of Twente, 7522 NB Enschede, The Netherlands

[a]s.s.mirhosseini@utwente.nl, [a]e.s.perdahcioglu@utwente.nl, [a]c.soyarslan@utwente.nl, [d]a.h.vandenboogaard@utwente.nl

Keywords: Computational Homogenization, Crystal Plasticity, Finite Strain, Finite Element Analysis, Voronoi Tessellation.

Abstract. In this paper, macroscopic behavior obtained from crystal plasticity finite element simulations of irregularly shaped 3D and 2D volume elements (VEs) are compared. These morphologically periodic VEs are generated using the open-source software library Voro++. Periodic boundary conditions are utilized to homogenize the material response employing a prescribed macroscopic deformation gradient tensor. To accelerate the assignment of periodic boundary conditions, a conformal mesh is employed by which periodic couples of faces on the hull of the volume element have identical mesh patterns. In the simulations, plane strain conditions are assumed, which means that the average thickness strain in 3D VEs is set to zero. However, grains are allowed to strain in the thickness direction. In the case of 2D VEs, plane strain elements are used. The principal goal of this comparison is to evaluate the accuracy of 2D VEs simulations. In the current study, two kinds of 2D VEs are generated: 1) Slicing 3D VEs normal to the thickness direction, 2) Separately generating 2D VEs. The first method corresponds to sectioning 3D microstructures using EBSD. This approach is generally used as an assumed more accurate alternative to 2D VEs. Based on the results, there is a large gap between the flow curves of 2D and 3D VEs. Additionally, 2D sectioning of 3D VEs does not necessarily end up in higher precision in material behavior predictions.

Introduction

Multiscale modelling is one of the most widely used methods to characterize the influence of heterogeneities in the microstructure on the response of the polycrystalline material. It is used as a bridge between various scales since macro-models are insufficient to express microstructural effects. The crystal plasticity finite element method (CPFEM) is one of the aforementioned numerical tools to capture the influence of mechanical anisotropy of crystals as well as intra-grain interactions on the local and global material behavior. This method is based upon the concept of representative volume elements (RVEs) first introduced by Hill [1]. It represents a material point with a finite size volume that is representative of material behavior at macroscale.

There are a vast number of studies focusing on the application of the crystal plasticity finite element method to various problems. Although many research studies emphasize on 2D RVEs with planar assumptions, the application of 3D RVEs has gained some attention recently. Lewis and Geltmacher [2] used a 3D spatial and crystallographic reconstruction of an austenitic steel microstructure using optical microscopy, serial sectioning, and electron backscatter diffraction. Kim et al. [3] used 3D RVEs to capture the Bauschinger effect in dual-phase steels. The generated model was utilized to simulate the mesoscale mechanical response of the real microstructure. Anbarlooie et al. [4], employed finite element based analysis of 2D and 3D RVEs to predict dual-phase steels response and damage initiation. Lim et al [5] performed large-scale CPFEM simulations on single and polycrystals to capture mesh sensitivity and RVE sizes. Christoudoulou et al. [6] investigated the impact of crystallographic orientation on the growth of intergranular voids using a dilatational visco-plasticity fast

Fourier transform-based framework. Mayeur and McDowell [7] used a 3D crystal plasticity model for Ti-6Al-4V. Their model was capable of reproducing the experimental data. In this study, it is remarked that the simplified 2D slip geometry models are insufficient to capture the full range of responses for Ti-64 since they do not account for all aspects of the texture. Ramazani et al. [8] used a correlation factor between 2D and 3D stresses since they found 2D modelling approaches not capable of obtaining the flow curve of material precisely. Besides, Thomser [9] shows that flow curves of 2D RVEs underestimate the experimental results. In the study of Qayyum et al. [10], 3D RVE simulation results are compared with those of 2D RVEs, constructed by slicing 3D RVEs in depth. Based on their study, 2D RVEs can be used in finite element simulations once the global deformation behavior is considered. However, 3D RVEs simulations are necessary to determine the local deformations accurately.

To summarize, the application of 2D RVEs seems to be inadequate to predict the realistic material behavior during deformation. In this paper, averaged macroscopic flow curves are compared for 2D and 3D irregularly shaped volume elements (VEs) using plane strain condition. The Voronoi-based volume elements are generated using Voro++ software library [11] and used in crystal plasticity finite element simulations. Plane strain condition in 3D is employed via setting the average thickness strain to zero. This assumption is activated by means of plane strain elements in 2D. To generate 2D VEs, sectioned 3D VEs normal to the thickness direction, as in the case of experimental practice, are used. In parallel, 2D VEs are generated independently; since the non-homogeneous grain size distribution over the 2D sections introduces an extra implicit resource of anisotropy. The results are also compared with the stress-strain plots of separately generated 2D VEs.

Theory

In this section, the governing equations for the utilized rate-independent finite strain crystal plasticity model that has been implemented as the user defined material model in finite element simulations is summarized [12].[1] Let referential and spatial configurations denoted by $\mathcal{B}_0$ and $\mathcal{B}$, respectively. The material points in the reference configuration $\mathcal{B}_0$ be denoted by $\boldsymbol{X} \in \mathcal{B}_0$ which are mapped onto points $\boldsymbol{x} \in \mathcal{B}$ at time $t \in \mathcal{R}_+$ in the current configuration $\mathcal{B}$ by the invertible nonlinear deformation map $\boldsymbol{\varphi}(\boldsymbol{X}, t)$ with $\boldsymbol{x} = \boldsymbol{\varphi}(\boldsymbol{X}, t)$. The deformation gradient $\boldsymbol{F}$ and its Jacobian determinant J are defined by $\boldsymbol{F} = \boldsymbol{\nabla}_0 \boldsymbol{\varphi}(\boldsymbol{X}, t) = \partial \boldsymbol{x} / \partial \boldsymbol{X}$ and $J = \det \boldsymbol{F}$, respectively. In the crystal plasticity model, plastic deformation occurs because of crystallographic slip that happens on slip systems whilst neglecting other deformation mechanisms such as twinning or transformation induced plasticity effects. Thus, $\boldsymbol{F}$ is decomposed multiplicatively into elastic part $\widehat{\boldsymbol{F}}_{\mathrm{e}}$, which represents elastic stretching and lattice rotation with reference to intermediate configuration, and plastic part $\boldsymbol{F}_{\mathrm{p}}$, which denotes the plastic deformation resulting from dislocation glide, as follows

$$\boldsymbol{F} = \widehat{\boldsymbol{F}}_{\mathrm{e}} \cdot \boldsymbol{F}_{\mathrm{p}} \,. \tag{1}$$

Using the definition of the total velocity gradient $\boldsymbol{L} = \dot{\boldsymbol{F}} \cdot \boldsymbol{F}^{-1}$ along with Eq. (1) amounts to the following additive decomposition into elastic $\widehat{\boldsymbol{L}}_{\mathrm{e}}$ and plastic $\widehat{\boldsymbol{L}}_{\mathrm{p}}$ parts

$$\boldsymbol{L} = \widehat{\boldsymbol{L}}_{\mathrm{e}} + \widehat{\boldsymbol{L}}_{\mathrm{p}} \,. \tag{2}$$

Letting the slip system α be defined with the two orthogonal unit vectors $\boldsymbol{s}^{(\alpha)}$ and $\boldsymbol{m}^{(\alpha)}$, which respectively denote the associated slip direction and the slip plane normal, and $\dot{\gamma}^{(\alpha)}$ denote the (positive)

[1] Let $\boldsymbol{a}$ and $\boldsymbol{b}$ denote two first-order, and $\boldsymbol{A}$ and $\boldsymbol{B}$, and $\boldsymbol{C}$ three second-order tensors. Using Einstein's summation convention on repeated indices, $\boldsymbol{C} = \boldsymbol{A} \cdot \boldsymbol{B}$ represents the single contraction product with $C_{ik} = A_{ij} B_{jk}$. $d = \boldsymbol{A} : \boldsymbol{B}$ represents the double contraction product with $d = A_{ij} B_{ij}$, where d is a scalar. $\mathbb{E} = \boldsymbol{A} \otimes \boldsymbol{B}$, $\mathbb{F} = \boldsymbol{A} \oplus \boldsymbol{B}$, and $\mathbb{G} = \boldsymbol{A} \ominus \boldsymbol{B}$ represent the tensor products with $\mathbb{E}_{ijkl} = A_{ij} B_{kl}$, $\mathbb{F}_{ijkl} = A_{ik} B_{jl}$, and $\mathbb{G}_{ijkl} = A_{il} B_{jk}$, where $\mathbb{E}$, $\mathbb{F}$, and $\mathbb{G}$ represent fourth-order tensors. The tensor product of $\boldsymbol{a}$ and $\boldsymbol{b}$ yields $\boldsymbol{A} = \boldsymbol{a} \otimes \boldsymbol{b}$ with $A_{ij} = a_i b_j$. $\dot{\boldsymbol{A}}$, $\boldsymbol{A}^{\top}$ and $\boldsymbol{A}^{-1}$ denote the material time derivative, the transpose, and the inverse of $\boldsymbol{A}$, respectively. $\mathrm{sym}(\boldsymbol{A})$ gives the symmetric part of $\boldsymbol{A}$ with $\mathrm{sym}(\boldsymbol{A}) = [1/2][\boldsymbol{A} + \boldsymbol{A}^{\top}]$. Finally, $\mathbf{1}$ denotes the second-order identity tensor.

Table 1: Selected material parameters for Aluminum with FCC crystal structure.

property	symbol	unit	magnitude
Young's modulus	E	[GPa]	72
Poisson's ratio	ν	$[-]$	0.33
Length of Burgers vector	b	[mm]	2.86×10^{-7}
Initial dislocation density	ρ_0	[mm^{-2}]	10^5
Saturation dislocation density	ρ_∞	[mm^{-2}]	10^{11}
Saturation shear strain	γ_∞	$[-]$	10
Initial critical resolved shear strength	τ_0	[MPa]	100

shear rate on the same slip system, the plastic part of the total velocity gradient tensor $\widehat{\boldsymbol{L}}_{\mathrm{p}}$ is given by the following sum [13, 14] over each slip system for $\alpha = 1, 2, \ldots n$

$$\widehat{\boldsymbol{L}}_{\mathrm{p}} = \sum_{\alpha=1}^{n} \dot{\gamma}^{(\alpha)}\, \boldsymbol{s}^{(\alpha)} \otimes \boldsymbol{m}^{(\alpha)} \,. \tag{3}$$

In order slip to be activated on the slip system α, the associated resolved shear stress should reach the associated slip resistance $\tau_{\mathrm{f}}^{(\alpha)}$ with $\varphi^{(\alpha)} = 0$ where $\varphi^{(\alpha)} = \tau^{(\alpha)} - \tau_{\mathrm{f}}^{(\alpha)} \leq 0$. The resolved shear stress is calculated using Schmid's law by projection of the (true) Cauchy stress tensor $\boldsymbol{\sigma}$ onto the slip system with $\tau^{(\alpha)} = \boldsymbol{s}^{(\alpha)} \cdot \boldsymbol{\sigma} \cdot \boldsymbol{m}^{(\alpha)}$.

A hypoelastic relation links the lattice corotational rate of Cauchy stress tensor $\overset{\triangledown}{\boldsymbol{\sigma}}$ to the elastic part of the rate of deformation tensor, which, in view of Eq. (2) is defined as $\boldsymbol{D}_{\mathrm{e}} := \mathrm{sym}(\widehat{\boldsymbol{L}}_{\mathrm{e}}) = \mathrm{sym}(\boldsymbol{L} - \widehat{\boldsymbol{L}}_{\mathrm{p}})$, with

$$\overset{\triangledown}{\boldsymbol{\sigma}} = \mathbb{C}_{\mathrm{e}} : \boldsymbol{D}_{\mathrm{e}} \,. \tag{4}$$

Here, $\mathbb{C}_{\mathrm{e}}$ denotes the constant elastic stiffness tensor. With assumption of elastic isotropy and the definitions $\mathbb{I}_{\mathrm{vol}} := [1/3]\mathbf{1}\otimes\mathbf{1}$, $\mathbb{I}_{\mathrm{dev}} := \mathbb{I} - \mathbb{I}_{\mathrm{vol}}$ and $\mathbb{I} = [1/2][\mathbf{1}\oplus\mathbf{1} + \mathbf{1}\ominus\mathbf{1}]$, we have $\mathbb{C}_{\mathrm{e}} := 3K\mathbb{I}_{\mathrm{vol}} + 2\mu\mathbb{I}_{\mathrm{dev}}$. Here, K and μ denote bulk and shear moduli, respectively, which are related to Young's modulus E and Poisson's ratio ν with $K = [1/3]E/[1-2\nu]$ and $\mu = [1/2]E/[1+\nu]$. The work-hardening is considered to happen by impediment of dislocation motion by increase of the forest dislocation density. Therefore, a Taylor-type hardening law [15] is used with

$$\tau_{\mathrm{f}}^{(\alpha)} = \tau_0 + \mu b \sqrt{\sum_{\beta=1}^{n} Q^{(\alpha\beta)} \rho^{(\beta)}} \,. \tag{5}$$

In Eq. (5), τ_0 is the lattice friction, b the Burgers vector length, $\rho^{(\beta)}$ the total dislocation density of the slip system β and $Q^{(\alpha\beta)}$ the interaction matrix between the slip systems which characterizes the strengthening of slip system α due to increase of dislocation density on slip system β.

Finally, the following saturation-type evolution equation determines the rate of dislocation density $\rho^{(\alpha)}$ on each slip system α

$$\dot{\rho}^{(\alpha)} = \frac{\dot{\gamma}^{(\alpha)}}{\gamma_\infty} [\rho_\infty - \rho^{(\alpha)}] \,. \tag{6}$$

At each slip system α, an identical initial dislocation density ρ_0 is assumed. Here ρ_∞ denotes saturation dislocation density whereas γ_∞ the saturation shear strain [16]. In this model, isotropic elasticity has been used, and the associated material parameters which have been used in the application problems of this work are listed in Table 1.

Numerical Studies

Microstructure Generation. In this step, arbitrarily shaped volume elements (VEs) are generated based on Voronoi tessellation using Voro++ [11]. Voro++ provides a radical Voronoi tessellation starting from a randomly generated set of seed points whose number corresponds to the number of cells obtained. In this research, a uniform size distribution in 3D is intended; therefore, the radius for each cell has been chosen as unity. However, due to the randomness involved in the location of seed points, this still results in a cell size distribution. Although this might be more realistic in comparison with an actual microstructure in the current numerical study, this introduces an unintentional (and not controlled) extra variance in cell size. In order to avoid this, Lloyd's algorithm [17] is implemented as an iterative tool to Voro++. This algorithm works by replacing the seed locations iteratively with the centroid of the generated cells. Consequently, after each iteration, the size of the cells becomes more uniform. There is, however, no check for stopping criteria relating to the uniformity of cell size; rather, a predetermined number of iterations are used with different initial seeds in obtaining a regularized structure. The number of iterations is referred to as the Lloyd factor in the following.

In the current study, a Lloyd factor of 300 has been chosen for unit cell generations. An example of the VEs with 125 grains that are not necessarily constrained in a cube is depicted in Fig. 1. The VEs are periodic, which means that for each of the exterior faces of the VE, there exists an identical face periodically placed on the other side of the hull. To apply periodic boundary conditions in Abaqus, a conformal mesh is generated by which the mesh pattern of each face on the hull is mapped to its pair. Once the VE is meshed, through prescribing a macroscopic deformation gradient tensor, the displacement of the periodically located nodes on the hull of the VE is constrained. Grains orientations are assigned using randomly generated but uniformly distributed Euler angles. Since this paper's primary goal is to compare the outcomes of crystal plasticity finite element simulations in 2D and 3D space, a cut of 3D VE perpendicular to thickness direction depicted in Fig. 2a has been made, Fig. 1(b). Based on this image, there exists heterogeneity in grain size distribution on the cut. Another 2D VE has been generated separately with the same number of grains per 3D VE length in each direction, Fig. 1(c). Afterward, the number of grains that possess a specific volume fraction is depicted in histogram bins in Fig. 2. Fig. 2(a) shows that grain size distribution is restricted within a short interval. According to this figure, for the cut of 3D VE (Fig. 2(b)), a wide grain size distribution is observed, whereas for the independently created 2D VEs (Fig. 2(c)), the grain size is distributed relatively uniform.

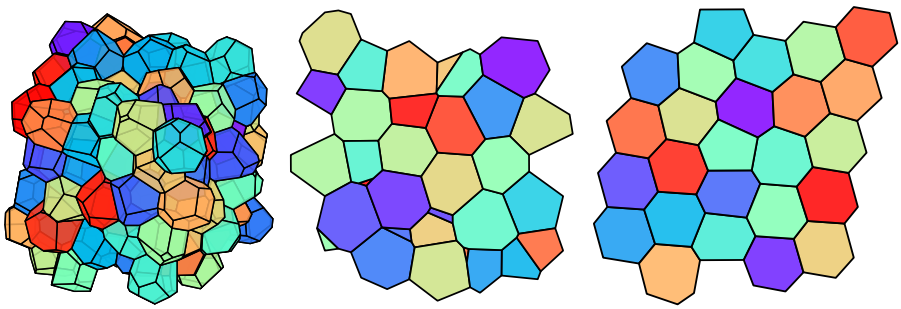

(a) (b) (c)

Fig. 1: Periodic volume elements used in this study. (a) 3D raspberry microstructure with 125 grains with a Lloyd factor of 300, (b) a 2D section of the 3D volume element (Lloyd=300), (c) Separately generated 2D raspberry microstructure with a Lloyd factor of 300. Fig. 2 gives associated grain size distribution.

Furthermore, inverse pole figures for the unit cells are illustrated as individual points depicting individual grain orientations in Fig. 4. According to this image, Euler angle distribution is almost uniform in the case of 3D VE, whereas there is a non-homogeneous distribution captured for 2D volume elements.

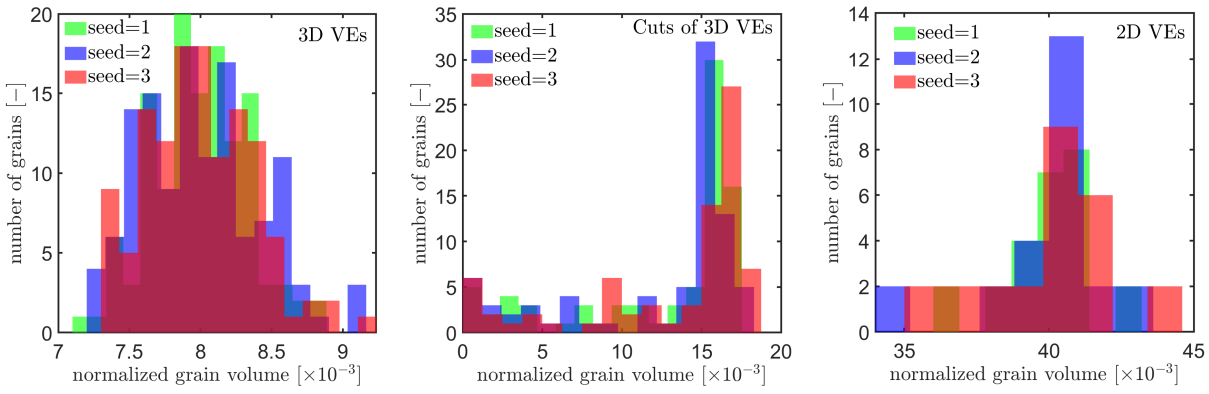

(a) (b) (c)

Fig. 2: Statistical overview of the number of grains versus their volume fraction for 3D sections and 2D volume elements (for 2D with a unit out-of-plane dimension assumption) generated separately and by means of sectioning 3D volume elements. The grain size varies considerably for each grain in the cut model although the background 3D generation has a higher uniformity.

Simulations with FEM. Once the model is generated, the behavior of the material is defined by means of the crystal plasticity model at individual integration points. For 3D VE simulations, plane strain condition is assumed, which means that although the individual grains are allowed to strain in the thickness direction, the average strain in the thickness direction is zero. It is worth mentioning that ten-node tetrahedral elements C3D10 have been used in these simulations. For the case of 2D simulations, six-node quadratic plane strain elements called CPE6 have been employed. Besides a final engineering strain of 0.1 has been prescribed in the loading direction. Once the simulations are accomplished, an averaging is performed on the strain and stress fields based upon the method introduced by [18].

Results and Discussions

Plane strain analysis results on 2D and 3D volume elements are implemented in this section. Three-dimensional VEs with $5 \times 5 \times 5$ grains are generated three times with randomly attributed grains orientations. Plane strain assumption is considered by which the average strain in the thickness direction is set to zero. In addition, 3D VEs are sectioned at mid-surface normal to the thickness direction. This procedure of creating 2D VEs is inspired by the standard experimental approach, which uses an Inverse Pole Figure (IPF) map from Electron Backscatter Diffraction (EBSD) analysis conducted on the sample cut plane. Afterwards, 2D VEs are generated independently with 5×5 grains. The averaged true stress versus true strain in the loading direction is displayed in Fig. 3. In this image, the mean value of three VEs in 3D and 2D, as well as the deviations, is depicted. Based on this figure, for 3D VEs, the deviation from the mean value is small, which means that $5 \times 5 \times 5$ grains in 3D can be representative of macroscopic material behavior, and the chosen volume element is representative. Fig. 3 implicates that three-dimensional VE is hardening much more noticeably compared to 2D ones. This behavior might be attributed to the additional slip that occurs in the thickness direction (average plane strain direction in 3D), but more research is necessary. As mentioned in the previous section, the assumption of plane strain in 3D is employed on the average strain in the thickness direction. It means that although the average plane strain condition holds, the grains are allowed to strain in the thickness direction. The extra slip in the 3D case results in higher statistically stored dislocations (SSDs) densities and higher hardening of the material compared to 2D plane strain simulations.

In the literature, sectioning 3D RVEs by means of EBSD is sometimes recommended as a replacement for independently generated 2D RVEs. This method is assumed to result is approximations closer to 3D ones. However, Fig. 3 shows that using 2D VEs that are generated as cuts of 3D using EBSD does not necessarily result in predictions that are closer to 3D hardening values.

In the elastic part, isotropic elasticity is used, which means that all simulations are expected to behave identically in this regime. In the elastic regime displayed in Fig. 3, all of the curves are overlapping as anticipated, and the slope of the elastic region (Fig. 3(a)) is higher than Young's modulus of the material. This slope can be found using Hooke's law in plane strain conditions. This slope can be simply computed using $E/[1-\nu^2] = 80.799$ GPa, which is equal to the prediction of this paper.

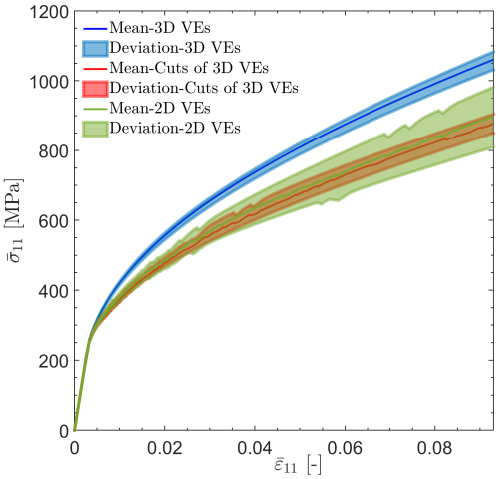

Fig. 3: Averaged true stress-true strain curves in the loading direction.

Conclusion

In this paper, crystal plasticity finite element simulations are implemented on three and two-dimensional irregularly shaped VEs. Plane strain assumption is used in the simulations to assess whether it gives an acceptable approximation of material behavior or not. Based on the outcomes, there is a significant discrepancy between the simulations in 2D and 3D space. On the other hand, the approach of using 2D cuts of the microstructure generated by EBSD images does not improve the approximations.

Acknowledgments

This research was carried out under project number T17019a in the framework of the Research Program of the Materials innovation institute (M2i) (www.m2i.nl) supported by the Dutch government and TATA Steel company.

Appendix

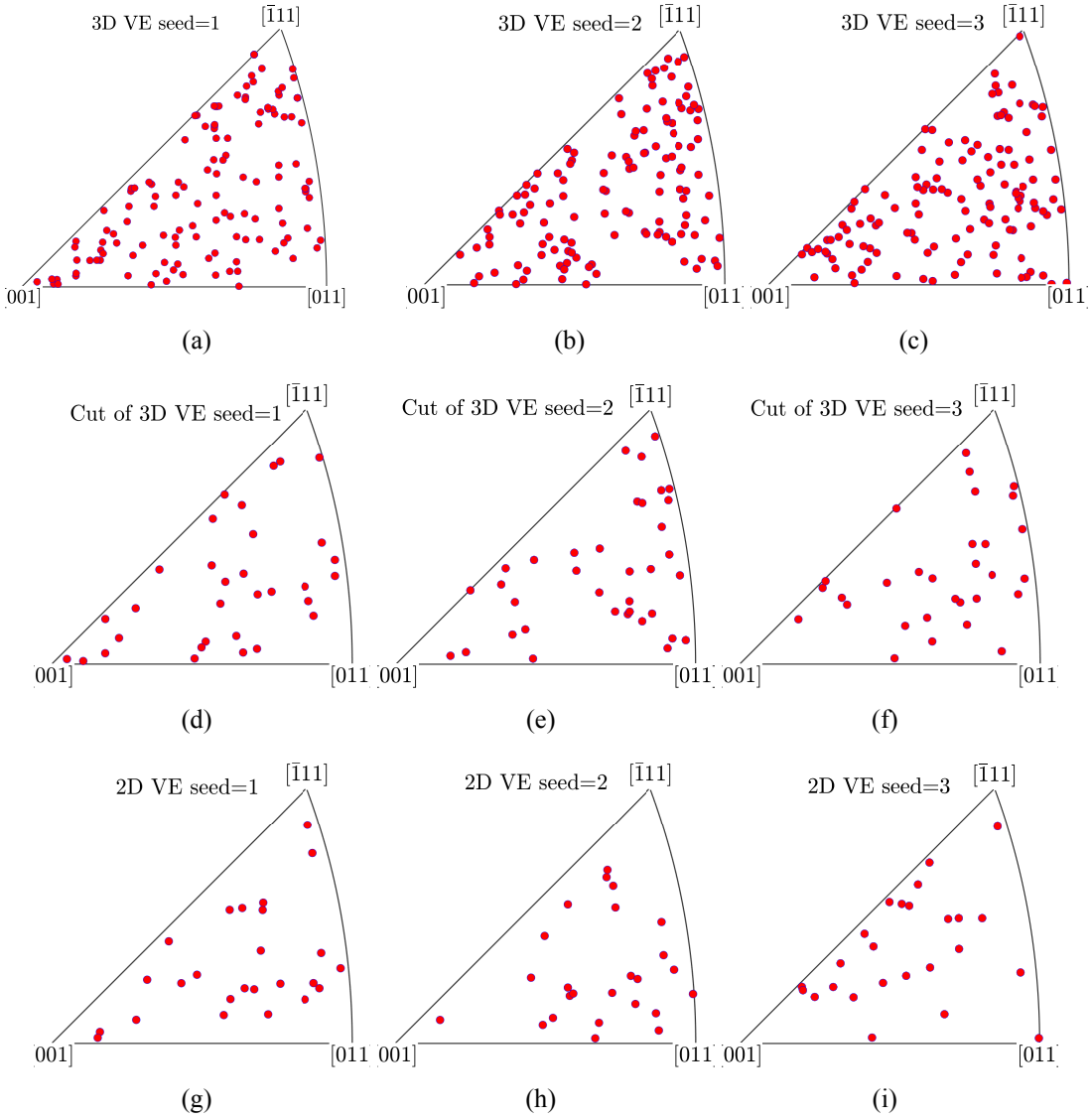

Fig. 4: Inverse pole figure displaying a point-wise distribution of grain orientations. (a) for the 125-grain 3D VEs, (b) 3D VE cuts and (c) separately generated 2D VE.

References

[1] R. Hill. “Elastic properties of reinforced solids: some theoretical principles”. In: *Journal of the Mechanics and Physics of Solids* 11.5 (1963), pp. 357–372.

[2] A. Lewis and A. Geltmacher. “Image-based modeling of the response of experimental 3D microstructures to mechanical loading”. In: *Scripta Materialia* 55.1 (2006), pp. 81–85.

[3] J. H. Kim et al. “Crystal plasticity approach for predicting the Bauschinger effect in dual-phase steels”. In: *Materials Science and Engineering: A* 539 (2012), pp. 259–270.

[4] B. Anbarlooie et al. “Experimental and 3D micromechanical analysis of stress–strain behavior and damage initiation in dual-phase steels”. In: *Journal of Materials Engineering and Performance* 28.5 (2019), pp. 2903–2918.

[5] H. Lim et al. “Investigating mesh sensitivity and polycrystalline RVEs in crystal plasticity finite element simulations”. In: *International Journal of Plasticity* 121 (2019), pp. 101–115.

[6] P. G. Christodoulou et al. “Role of crystallographic orientation on intragranular void growth in polycrystalline FCC materials”. In: *International Journal of Plasticity* 147 (2021), p. 103104.
[7] J. Mayeur and D. McDowell. “A three-dimensional crystal plasticity model for duplex Ti–6Al–4V”. In: *International journal of plasticity* 23.9 (2007), pp. 1457–1485.
[8] A. Ramazani et al. “Correlation between 2D and 3D flow curve modelling of DP steels using a microstructure-based RVE approach”. In: *Materials Science and Engineering: A* 560 (2013), pp. 129–139.
[9] C. Thomser. “Modelling of the mechanical properties of dual phase steels based on microstructure [Ph. D. thesis]”. In: *RWTH-Aachen, Germany* (2009).
[10] F. Qayyum et al. “Effect of 3D representative volume element (RVE) thickness on stress and strain partitioning in crystal plasticity simulations of multi-phase materials”. In: *Crystals* 10.10 (2020), p. 944.
[11] C. H. Rycroft. *A three-dimensional Voronoi cell library in C++*. Tech. rep. LBNL-1432E. Lawrence Berkeley National Laboratory, Feb. 2009.
[12] E. Asik, E. Perdahcioglu, and T. van den Boogaard. “An RVE-Based Study of the Effect of Martensite Banding on Damage Evolution in Dual Phase Steels”. English. In: *Materials* 13.7 (Apr. 2020).
[13] J. Mandel. “Généralisation de la théorie de plasticité de WT Koiter”. In: *International Journal of Solids and structures* 1.3 (1965), pp. 273–295.
[14] J. R. Rice. “Inelastic constitutive relations for solids: an internal-variable theory and its application to metal plasticity”. In: *Journal of the Mechanics and Physics of Solids* 19.6 (1971), pp. 433–455.
[15] G. I. Taylor. “The mechanism of plastic deformation of crystals. Part I.—Theoretical”. In: *Proc. R. Soc. Lond. A* 145.855 (1934), pp. 362–387.
[16] M. Becker. “Incompatibility and instability based size effects in crystals and composites at finite elastoplastic strains”. PhD thesis. Institut für Mechanik (Bauwesen), Lehrstuhl I, 2006.
[17] S. P. Lloyd. “Least Square Quantization in PCM”. In: *IEEE transcation o information theory* IT-28.2 (Mar. 1982), pp. 129–137.
[18] V. Kouznetsova, W. Brekelmans, and F. Baaijens. “An approach to micro-macro modeling of heterogeneous materials”. In: *Computational mechanics* 27.1 (2001), pp. 37–48.